

Zn_xZr/HZSM-5 as efficient catalysts for alkylation of benzene with carbon dioxide

Junjun Cheng, Yitao Zhao, Guohao Xu, Peng Zhang, Xuedong Zhu (✉), Fan Yang

Engineering Research Center of Large-Scale Reactor Engineering and Technology, Ministry of Education, East China University of Science & Technology, Shanghai 200237, China

© Higher Education Press 2022

Abstract Alkylation of benzene with carbon dioxide and hydrogen to produce toluene and xylene could increase the added-value of surplus benzene as well as relieve environmental problems like green-house effect. In this work, the alkylation benzene with carbon dioxide and hydrogen reaction was proceeded by using the mixture of zinc-zirconium oxide and HZSM-5 as bifunctional catalyst. The equivalent of Zn/Zr = 1 displays the best catalytic performance at 425 °C and 3.0 MPa, and benzene conversion reaches 42.9% with a selectivity of 90% towards toluene and xylene. Moreover, the carbon dioxide conversion achieves 23.3% and the carbon monoxide selectivity is lower than 35%, indicating that more than 50% carbon dioxide has been effectively incorporated into the target product, which is the best result as far as we know. Combined with characterizations, it indicated that the Zn and Zr formed a solid solution under specific conditions (Zn/Zr = 1). The as-formed solid solution not only possesses a high surface area but also provides a large amount of oxygen vacancies. Additionally, the bifunctional catalyst has excellent stabilities that could keep operating without deactivation for at least 80 h. This work provides promising industrial applications for the upgrading of aromatics.

Keywords carbon dioxide, alkylation of benzene, solid solution catalyst, bifunctional catalyst

1 Introduction

The unprecedented rise in greenhouse gas emission is considered to be a major contributor to the global climate change and ocean acidification [1]. The greenhouse gas of most significance, CO₂, is viewed as a breakthrough point

in curbing climate warming. CO₂ is actually a non-toxic and carbon source in abundance, which provides an option to synthesize carbon-containing compounds [2–7]. For example, with the help of hydrogen, the conversion of CO₂ into high value-added and commercialized chemicals can alleviate environmental problems caused by excessive carbon emissions [8,9]. On the other hand, the demand for more eco-friendly fuels has rigorous restrictions on the compositions of gasolines, leading to the redundancy of benzene. Therefore, it is urgent to combine the conversion of CO₂ with benzene to produce several value-added products, among which toluene and xylene are the most significant basic organic chemical raw materials [10]. To name but a few, toluene is mainly used as the organic solvent, gasoline additives and precursor of benzoic acid while xylene is mainly used in the production of polyester, resin, fiber, and coatings. In particular, para-xylene is used in the production of 1,4-dicarboxybenzene and further for the synthesis of polyethylene glycol terephthalate, which is a widely used thermoplastic polyester with great economic potential [11,12].

The selective synthesis of para-xylene through benzene alkylation with methanol has been extensively studied recently [13–17]. The rate-determining step of the reaction is to overcome the high energy barrier to the conversion of methanol to methoxy (CH₃O*) substances. Thus, an efficient methylation reagent rapidly generating surface CH₃O* is necessary for benzene alkylation. Using the greenhouse gas CO₂ combined with renewable H₂ as methyl source is considered to be a better route [18]. In the alkylation of benzene with carbon dioxide and hydrogen (ABCH) reaction, the CO₂/H₂ mixture as a methylation reagent to rapidly produce CH₃O* on metal oxides is taken into account, followed by the transportation of CH₃O* species onto zeolite, which affords the alkylation of CH₃O* and benzene. Compared with alkylation of benzene with methanol, ABCH could efficiently employ CO₂ as methyl resource and the existence of CO₂/H₂ has the potential to accelerate the

whole alkylation process. Additionally, the ABCH reaction has advantages over other pathways for the synthesis of xylene, such as succinct reaction route and circumvented thermodynamic limitations.

Bifunctional catalysts composed of metal oxides and molecular sieve are mainly used for the the ABCH reaction. Recently, Ting et al. reported Re/TiO₂ integrated H-MOR [19], Re/TiO₂ integrated H-β [20], and Pt/MoO_x/TiO₂ [21] integrated H-MOR as bifunctional catalysts in a batch reactors to catalyze the alkylation reactions of various aromatics. However, the cost of rhenium and the restrictions of batch reactors are not suitable for large-scale industrial production. Besides, Zuo [22] and Miao [23] reported the catalytic methylation of toluene using CO₂ and H₂ over a mixture of ZnZrO_x-ZSM-5 catalyst for the synthesis of para-xylene on fixed-bed reactors. More recently, Liu et al. [24] also detailed the alkylation of benzene over a mixture of ZnO/TiO₂ and HZSM-5 catalyst on a fixed-bed reactor, discussing the effect of molecular sieve acidity on the reaction. The catalysts used in the reaction of benzene/toluene with CO₂ and H₂ are believed to play two major roles, in which metal oxides contribute to the activation of carbon dioxide into intermediates, and molecular sieves are used to catalyze the alkylation of aromatics with intermediates. The main issues remaining to be solved are to find and develop inexpensive and non-toxic catalysts, to increase the conversion of benzene and CO₂ to the greatest possible extent, to inhibit CO₂ methanation and benzene de-aromatization and to increase the effective utilization of CO₂ to the greatest possible extent, as well as exploring the complete reaction mechanism of the reaction.

In this work, a highly active bifunctional catalyst composed of Zn/Zr metal oxide and HZSM-5 was developed by co-precipitant and physical mixing. It shows that Zn/Zr metal oxide enables the formation of a solid solution only under specific compositions. The as-formed solid solution owns the most oxygen vacancies, which is beneficial for the activity and CO₂ utilization. Moreover, the mechanism studies of reaction also demonstrate that carbon dioxide chemisorption on the oxygen vacancies generates carbonate/bicarbonate species undergoing stepwise hydrogenation to give formate (HCOO*), CH₃O*, and methanol, which are rapidly transferred to the acidic site of HZSM-5 to produce target products such as toluene and xylene by reaction with benzene.

2 Experimental

2.1 Chemical reagents and materials

Zn(NO₃)₂·6H₂O, Zr(NO₃)₄·5H₂O, (NH₄)₂CO₃, and benzene (analytically pure) were provided by Aladdin

company. HZSM-5 zeolite (Si/Al = 30) was purchased from Nankai University Catalyst Plant. Mixed gas containing CO₂, H₂, and N₂ (N₂:H₂:CO₂ = 1:3:1) was purchased from Air Liquide (China) Investment Co. LTD. All the reagents were utilized directly without further purification.

2.2 Preparation of catalysts

Zn_xZr oxides were prepared by the co-precipitant method. Briefly, certain amounts of Zn(NO₃)₂·6H₂O and Zr(NO₃)₄·5H₂O were dissolved in distilled water, and then (NH₄)₂CO₃ aqueous solution was added dropwise to the aforementioned solution under vigorous stirring till pH = 7. After being aged at 70 °C for 3 h, the precipitate was centrifuged and washed with distilled water. Next, the acquired products were dried at 110 °C for 12 h, followed by calcination at 500 °C for 6 h. These Zn/Zr oxides are named as Zn_xZr in the following, wherein the “x” represents the Zn/Zr molar ratio (0.5, 1.0, 2.0).

In the catalytic evaluation of the ABCH reaction, the bifunctional catalyst containing Zn_xZr oxides and HZSM-5 zeolites was prepared by physical mixing method. Typically, Zn_xZr and HZSM-5 were mixed by grinding using a mass ratio of 1:1. Then the obtained mixture was granulated into 20–40 mesh particles and calcined in 500 °C for 5 h with a ramping rate of 2 °C·min⁻¹ in a muffle furnace. The mixture is expressed as Zn_xZr-ZSM-5.

2.3 Characterizations

X-ray diffraction (XRD) was measured on D8 Advance (German Brook AXS Co., Ltd.), which was operated at 100 mA and 40 kV using Cu/Kα (λ = 1.5418 Å) as X-ray source. The diffraction patterns within 2θ ranging from 5° to 80° were collected with a scanning speed of 10 (°)·min⁻¹.

High resolution transmission electron microscope (HRTEM) and energy dispersive spectrum (EDS) data were recorded using a JEM-2100 transmission electron microscope.

N₂ physisorption experiments were carried out on ASAP 2020 (Micromeritics, USA). The calcined sample (approximately 100 mg) was degassed at 593 K under vacuum (< 0.1 Pa) for 24 h prior to measurement. N₂ adsorption was proceeded at 77 K using liquid nitrogen as coolant to obtain the corresponding adsorption–desorption isotherms. The specific surface area was calculated by the Brunauer–Emmett–Teller (BET) method. Surface areas and volumes of micropores were determined by the *t*-plot method.

Inductively coupled plasma atomic emission spectrometer (ICP-AES, manufactured in Agilent, USA) was used to determine the accurate Zn/Zr ratios of the Zn_xZr catalysts.

Raman spectra were performed on a Renishaw Micro

Raman spectrometer, the surface and bulk phase structures of the catalysts were detected at 325 and 785 nm.

X-ray photoelectron spectra (XPS) were acquired on an ESCALAB 250 spectrometer (Thermo Fish Scientific, Al $K\alpha$, $h\nu = 1486.6$ eV). The binding energy was corrected by C1s orbital, which was set at 284.8 eV. The software XPSpeak41 was used for data analysis. ‘Exposed O2’ was defined as the multiplication of surface O atom ratio, surface area and surface O2 ratio to estimate the absolute content of the available oxygen vacancies. Specific calculation values were shown in Table S1 (cf. Electronic Supplementary Material, ESM).

The H_2 temperature-programmed reduction (H_2 -TPR) experiments were carried out on a Micromeritics Chemisorb 2720 analyzer. The oxide tested was heated to 250 °C in a stream of Ar at a heating rate of 10 °C·min⁻¹ for half an hour to remove the adsorbed impurities. After cooling to 50 °C, the gas was switched to a 10% H_2 /Ar flow (10 mL·min⁻¹) and the sample was heated to 900 °C at a heating rate of 10 °C·min⁻¹. The signal was recorded by a thermal conductivity detector (TCD).

In-situ infrared spectroscopy experiments were measured using a Thermo Fisher Nicolet iS50 spectrometer equipped with an MCT detector and a high temperature reaction chamber with a CaF_2 window. The spectra were collected in the range of 4000–1300 cm⁻¹ by accumulating 32 scans at a 4 cm⁻¹ resolution.

2.4 Catalytic evaluation

In a representative catalytic evaluation of ABCH reaction, 1 g catalyst pellets were loaded into a 304 stainless steel tube and the rest was filled with quartz sands. Before each test, the catalyst was firstly pre-treated with H_2 at 450 °C, 1 atm (1.013×10⁵ Pa) for 1 h. Then the pressure was adjusted to 3.0 MPa by a backpressure valve and the temperature was switched to 425 °C. Afterwards, CO_2/N_2 and H_2 flow was introduced using mass flow controllers. Meanwhile, benzene was also injected into the reactor using a high pressure constant flow pump, bringing about

an approximate molar ratio of $12H_2:4CO_2:1C_6H_6$, corresponding to a gas hourly space velocity of 9000 mL·h⁻¹·g_{cat}⁻¹ and liquid hourly space velocity of 1.8 h⁻¹. The gas phase was analyzed using an on-line Agilent 8890 gas chromatograph equipped with a flame ionization detector connected to a PLOT-Q capillary column (30 m) and a TCD detector connected to a TDX-02 packed column (2 m). The liquid phase was collected and weighed every 2 h, analyzed by an off-line Agilent 8890 gas chromatograph equipped with a flame ionization detector connected to a DB-WAX capillary column (30 m).

3 Results and discussion

3.1 Characterization of metal oxides and bifunctional catalysts

The XRD patterns of the Zn_xZr oxides are illustrated in Fig. 1. Pure ZrO_2 prepared by co-precipitation is mainly the monoclinic ZrO_2 (m- ZrO_2) phase with some tetragonal ZrO_2 (t- ZrO_2) phase [25], displaying diffraction peaks at 28.3°, 31.6°, 34.1°, 35.3°, 50.1°, and 59.4° (Fig. 1(a)). With the addition of Zn, ZrO_2 changes from the mixed phase to the t- ZrO_2 dominated phase as evidenced by diffraction peaks at 30.2°, 50.7°, and 60.2°. ZnO phase can be unambiguously discerned in all Zn-contained samples and XRD intensities of ZnO phase at 31.8°, 34.5°, and 36.3° are gradually conspicuous with more Zn content, except for $Zn_{1.0}Zr$ which solely presents an m- ZrO_2 phase, implying the successful formation of the ZnO– ZrO_2 solid solution. Figure 1(b) is obtained by zooming in the 28°–38° interval with the highest peak intensity in Fig. 1(a). The peak position of the (101) plane on ZrO_2 is at 30.24°, while the peak position shifts to 30.45° for samples with Zn additions. The peaks at other positions also switch to higher diffraction angles to the same degree, indicating the reduction in the interplanar spacings of Zn_xZr oxide. As reported, the radius of Zn^{2+}

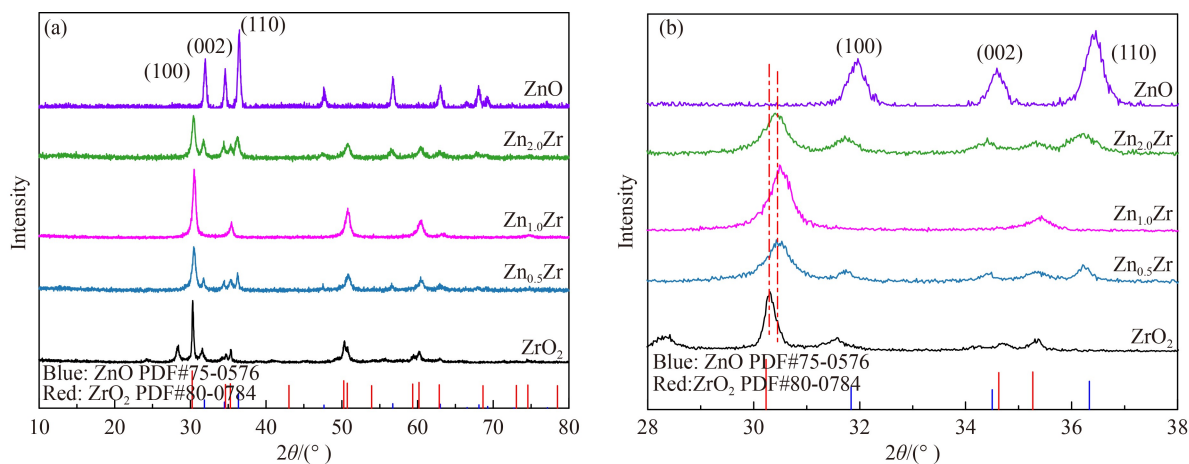


Fig. 1 XRD patterns of Zn_xZr oxides: (a) 10°–80°; (b) 28°–38°.

(0.74 Å) is smaller than that of Zr⁴⁺ (0.82 Å) [26], thus, the movements towards high diffraction angles substantiate the successful incorporation of Zn into the structures of ZrO₂ which according to Bragg's law [27,28]. This indicates that there are bimetal oxide solid solutions for all Zn/Zr samples, yet, it is more abundant in Zn_{1.0}Zr compared to others pertaining to the absence of ZnO phase.

To further prove the formation of solid solution for Zn_{1.0}Zr, Fig. 2 shows the HRTEM image. The interplanar spacing of Zn_{1.0}Zr is about 0.29 nm (Fig. 2(c)), which is attributed to the t-ZrO₂. Elemental mapping analysis confirms that Zn and Zr are homogeneously dispersed without obvious phase segregations. This also confirms that Zn_{1.0}Zr exists in solid solution, unlike other samples.

Table 1 lists the textural properties of various Zn_xZr oxides. The specific surface area of pure ZrO₂ and ZnO is comparatively smaller, which is 15 and 26 m²·g⁻¹, respectively. However, the surface areas increase slightly after Zn addition, which are about 36 m²·g⁻¹ for all Zn_xZr samples despite of various Zn/Zr ratios. The Zn/Zr ratios in the bulk phase measured by ICP-AES were close to the feed ratios, while the Zn/Zr ratios on the surface measured by XPS were significantly higher than those in the bulk phase, demonstrating the enrichment of Zn on

the catalyst surface during the preparation process.

Raman spectroscopy was used to further investigate the structure of the Zn_xZr oxides (Fig. 3). Raman spectroscopy with different laser sources could detect phases of different thickness, owing to light absorption and light scattering effects. The Raman peaks at 305, 333, 383, 477, 536, 560, 617, and 636 cm⁻¹ are obviously resolved for m-ZrO₂ under a 325 nm light source [29], indicating the predominant existence of m-ZrO₂. Besides, a peak at 269 cm⁻¹ regarded as the characteristic of t-ZrO₂ is also detected [30], demonstrating the hybrid nature of ZrO₂ in this research, which is in consistent with the XRD results. After the introduction of zinc, a typical peak at 564 cm⁻¹ substituted all original peaks, denoting to the transformation into cubic ZrO₂ phase. For the 785 nm, no obvious peaks can be found in ZrO₂ possibly due to the low sensitivity of longer wavelengths. However, after the introduction of zinc, the Raman peaks at 269, 316, 474, and 640 cm⁻¹ are obviously resolved for t-ZrO₂ under a 785 nm light source. These results indicate that ZrO₂ is the tetragonal phase within the main body of Zn_xZr but the surface changed into cubic ZrO₂ phase with the help of Zn. It should be emphasized, the peak at 322 cm⁻¹ standing for ZnO using 325 nm was not very

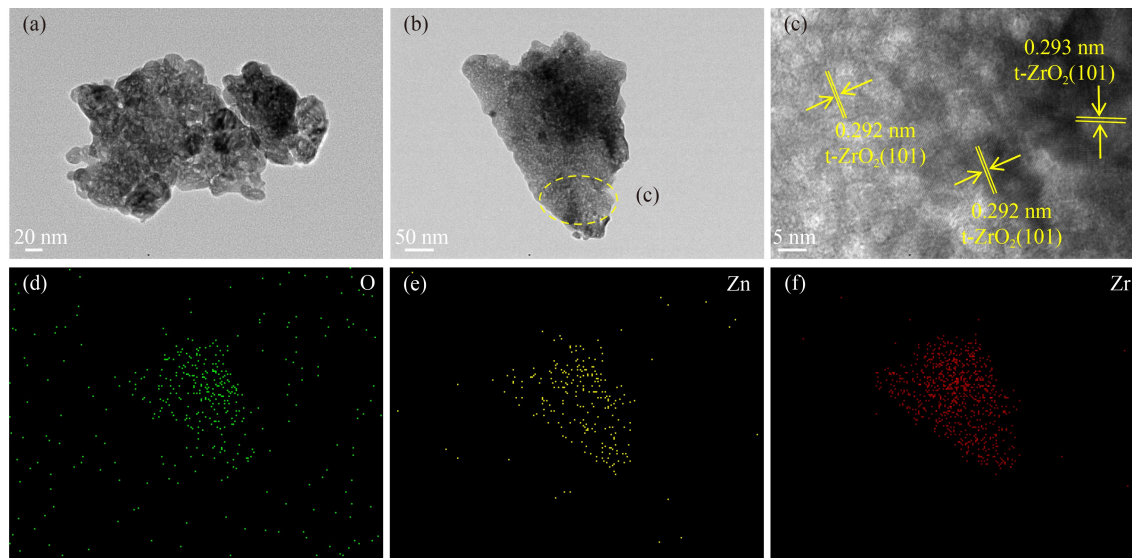


Fig. 2 (a–c) Zn_{1.0}Zr oxide HRTEM and (d–f) the corresponding EDS-mapping images that correspond to the image (b) and (d) O, (e) Zn, (f) Zr.

Table 1 Textural properties and surface compositions of the catalysts

Sample	$A_{\text{BET}}/(\text{m}^2 \cdot \text{g}^{-1})$	$D_{\text{pore}}/\text{nm}$	$V_{\text{pore}}/(\text{cm}^3 \cdot \text{g}^{-1})$	Zn/Zr molar ratio	
				Bulk ^{a)}	Surface ^{b)}
ZrO ₂	15	14.09	0.05	–	–
Zn _{0.5} Zr	38	10.67	0.10	0.46	1.34
Zn _{1.0} Zr	39	11.80	0.09	0.84	2.82
Zn _{2.0} Zr	36	23.90	0.21	1.45	4.61
ZnO	26	31.09	0.19	–	–

a) Zn/Zr molar ratios in the bulk were determined by ICP-AES; b) Zn/Zr molar ratios on the surface were determined by XPS.

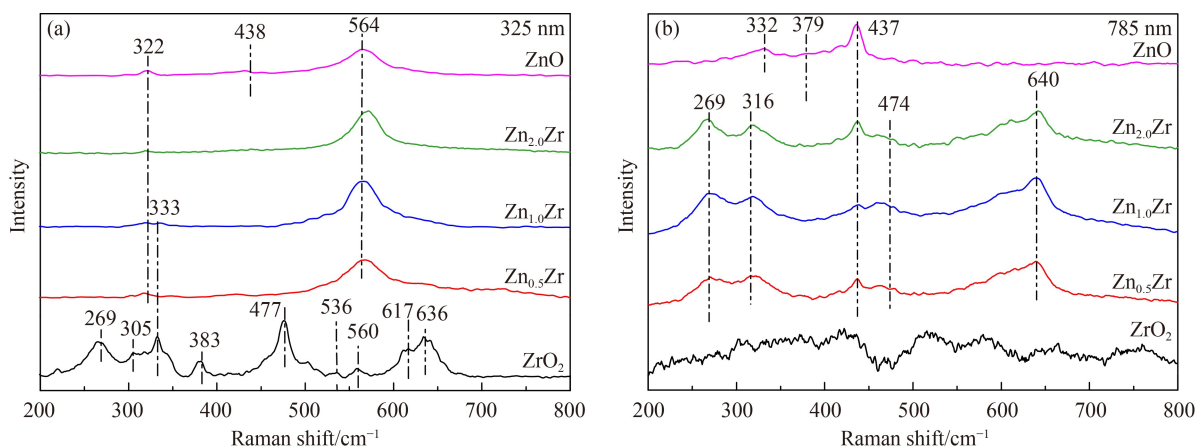


Fig. 3 Raman spectroscopies of Zn_xZr oxides used different laser sources: (a) 325 nm; (b) 785 nm.

significant while the peak at 332 cm^{-1} using 785 nm was not detected in other Zn_xZr samples [31,32]. This demonstrates there were several tiny ZnO phases on the surface of Zn_xZr oxides rather than in the bulk because of the surface enrichment effect. That exactly agrees with the results of ICP-AES and XPS in Table 1.

H_2 -TPR experiments were carried out to investigate the reduction of Zn_xZr catalysts and the interactions between the different components. As shown in Fig. 4, pure ZrO_2 shows a hydrogen consumption peak at about $490\text{ }^\circ\text{C}$, corresponding to the reduction of Zr^{4+} to Zr^{3+} [33]. The addition of Zn caused a significant shift in the surface reduction process towards lower temperatures. The Zn_xZr oxides show a hydrogen consumption peak at about $330\text{ }^\circ\text{C}$, while ZrO_2 gives a hydrogen consumption peak at about $490\text{ }^\circ\text{C}$. It indicates that Zn_xZr is more readily reduced and the catalyst is predominantly present as an oxide under the reaction conditions.

The surface elemental content and the chemical valence of the metal in the Zn_xZr oxides were investigated by XPS spectroscopy as depicted in Fig. 5. Figure 5(a) shows the Zn 2p XPS spectrum. Due to the spin split of the Zn 2p orbital, the XPS spectrum splits into two spin splitting peaks of Zn $2p_{1/2}$ and Zn $2p_{3/2}$ at around 1044.7 and 1021.7 eV [34,35], respectively. The peak of Zn $2p_{3/2}$ shifts towards a lower binding energy when the content of Zn increases, indicating a stronger interaction between ZrO_2 and ZnO at lower ZnO content [36]. Figure 5(b) shows the Zr 3d XPS spectrum. The XPS spectrum splits into two spin splitting peaks of Zr $3d_{5/2}$ and Zr $3d_{3/2}$ at 182.1 and 184.4 eV, respectively. The peak at 182.1 eV for Zr $3d_{5/2}$ in the pure ZrO_2 sample is attributed to the Zr^{4+} cation. The peak positions for Zr were generally consistent in all samples. Figure 5(c) shows the O 1s XPS spectrum. The oxygen vacancy on the metal catalyst can be deduced from the O 1s pattern. Three peaks locating at 530.2, 531.4, and 532.3 eV representing the O1, O2 and O3 species [37] respectively are fitted into the O 1s XPS spectra. The peak at 530.2 eV belongs to oxygen (O1) in the ZnO and ZrO_2 lattice [38], indicating oxygen in the

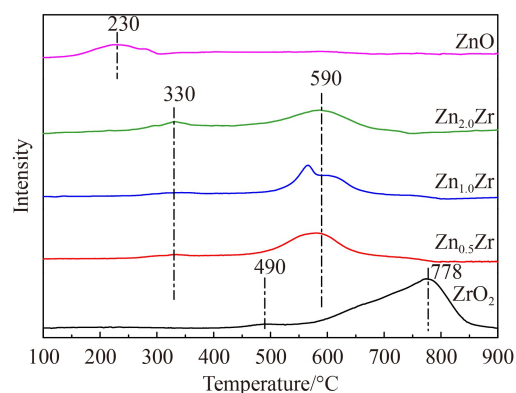


Fig. 4 H_2 -TPR of Zn_xZr oxides.

form of O^{2-} within the oxide lattice which occupies most of the surface oxygen. O2 at 531.4 eV and O3 at 532.3 eV are assigned to less charged oxygen anions and dissociatively chemisorbed oxygen, respectively, which are regarded as oxygen vacancies and surface defects [39]. The contents of lattice oxygen (O1) are 78.7% in ZnO and 79.8% in ZrO_2 , the other two oxygen species only make up 20%. For $Zn_{1.0}Zr$, the total O2 and O3 increase to 30.3%, while O1 decreases to 69.7%. This indicates there are more oxygen vacancies in $Zn_{1.0}Zr$ and the interaction between Zr and Zn is more intense.

From all the above analysis, it can be seen that the addition of Zn promotes the transformation of surface ZrO_2 into cubic phase. $Zn_{1.0}Zr$ solid solution shows a core-shell like structure consisting a cubic ZrO_2 shell enriched by ZnO, and an m- ZrO_2 core, while other samples contain agglomerated ZnO or segregation phases. Due to the special structure of $Zn_{1.0}Zr$, it exhibits more oxygen vacancies as evidenced by XPS.

3.2 Catalytic evaluation

3.2.1 Effects of metal oxides

Table 2 shows the experimental results on the distribution

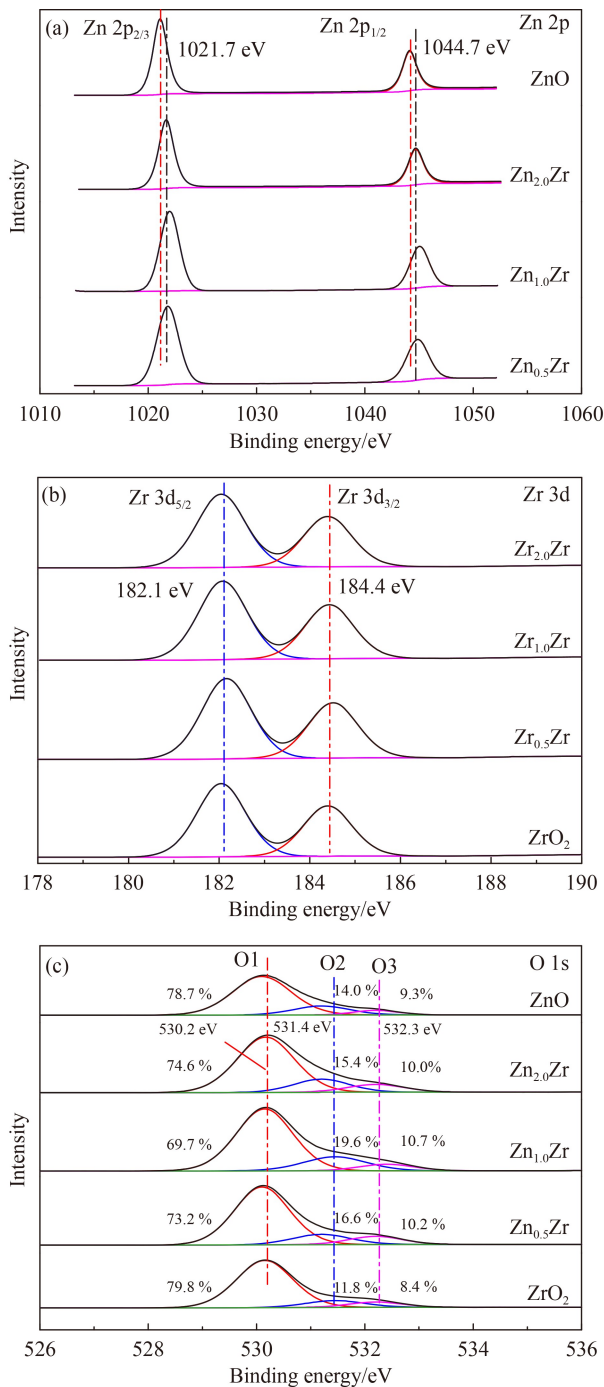


Fig. 5 XPS spectrums of (a) Zn 2p; (b) Zr 3d; (c) O 1s orbitals.

and selectivity of the liquid phase products in ABCH over bifunctional catalysts afforded by the mixture of Zn_xZr oxides and HZSM-5. In Table 2, the benzene conversions are 22.1% and 5.7% for ZnO-ZSM-5 and ZrO₂-ZSM-5, respectively, while Zn_xZr-ZSM-5 shows a significant increase in benzene conversion. Benzene conversion of Zn_{0.5}Zr-ZSM-5 is 41.8% and it increases to 42.9% in Zn_{1.0}Zr-ZSM-5 with excess zinc, then it reduces to 39.1% in Zn_{2.0}Zr-ZSM-5. In terms of selectivity, toluene occupies the majority of the products, accounting for

68.8%–93.3%, followed by xylene which is 2.6%–20.8%. The selectivity of toluene is higher than that of xylene, possibly resulting from the consecutive alkylation nature of xylene synthesis. The main by-products in the liquid phase are ethylbenzene and C₉₊, which account for less than 10%. The utilization of the benzene is also above 90%, indicating that the phenyl ring is successfully involved in the alkylation process, and side reactions are fully suppressed (such as benzene hydrogenation and thermal cracking).

Table 3 shows the product distributions of gas phase. The lowest CO₂ conversion is 10.9% for ZrO₂-ZSM-5, while the CO₂ conversions of the rest catalysts are rather close, which are about 25%. The CO selectivities of ZnO-ZSM-5 and ZrO₂-ZSM-5 were 72.0% and 84.1% respectively, while the CO selectivity of Zn_xZr-ZSM-5 shows a significant decrease. The CO selectivity of Zn_{1.0}Zr-ZSM-5 is 35.8% and the effective CO₂ utilization is as high as 50.9%. The remaining by-products are mainly methane and a small amount of C₂–C₄ hydrocarbons, with no methanol or dimethyl ether observed. Concerning the relative higher benzene conversion and lower CO selectivity, it can be inferred that Zn_{1.0}Zr displays a better alkylation ability mainly via the refrained reverse water gas shift reaction, which inhibits the transformation of CO₂ into CO, instead by more methanol intermediates [40]. The carbon balance values in Table 3 indicate that the catalyst system has a low carbon build-up and good catalyst stability during the reaction.

Figure 6 reveals the relationship between catalytic performances and the exposed O2. The horizontal coordinates of the graph represent the exposed O2, the samples contain more oxygen vacancies also show more exposed O2, while the vertical coordinates show the conversion of carbon dioxide or benzene as well as the benzene ring utilizations. As can be seen from the graph, within the range of exposed O2 = 1–7, there is a linear relationship between the activity of the catalyst and the O2 exposed by the oxide, the conversion of benzene and CO₂ increases almost linearly with exposed O2. Based on all the above findings, it can be concluded that for Zn_{1.0}Zr, the addition of a suitable amount of ZnO to ZrO₂ forms a Zn/Zr solid solution with Zn enriched cubic ZrO₂ shell and m-ZrO₂ core, this specific structure results in more oxygen vacancies. Oxygen vacancies were responsible for the adsorption and activation of CO₂ [40,41], leading to more intermediates and less CO, which further promotes the catalytic performances. The moderate addition of ZnO also acts as an active site to provide dissociated hydrogen for CO₂ hydrogenation, as reported previously [40]. The imbalanced Zn/Zr ratios of other Zn_xZr samples contain less solid solution and lead to ZnO clusters or hybrid ZrO₂ phases, which are unable to form abundant oxygen vacancies as active sites for the CO₂ conversion, showing unsatisfied catalytic results.

Table 2 Conversion of benzene and composition of the liquid phase^{a)}

Catalyst	Conversion/%		Selectivity/%				Phenyl ring yield ^{b)/%}
	Benzene	Toluene	Xylene	EBZ ^{c)}	C ₉₊	PX/X ^{d)}	
ZrO ₂ -ZSM-5	5.7	93.3	2.6	3.2	1.0	23.2	98.9
Zn _{0.5} Zr-ZSM-5	41.8	69.1	20.4	4.1	6.4	24.5	90.7
Zn _{1.0} Zr-ZSM-5	42.9	68.8	20.8	4.4	6.0	24.5	90.5
Zn _{2.0} Zr-ZSM-5	39.1	71.7	18.6	3.9	5.8	24.5	91.4
ZnO-ZSM-5	22.1	85.6	9.7	2.7	2.1	23.9	95.6

a) Reaction conditions: temperature = 425 °C, pressure = 3 MPa, H₂:CO₂ = 3:1, GHSV = 9000 mL·g⁻¹·h⁻¹, LHSV = 1.8 h⁻¹;

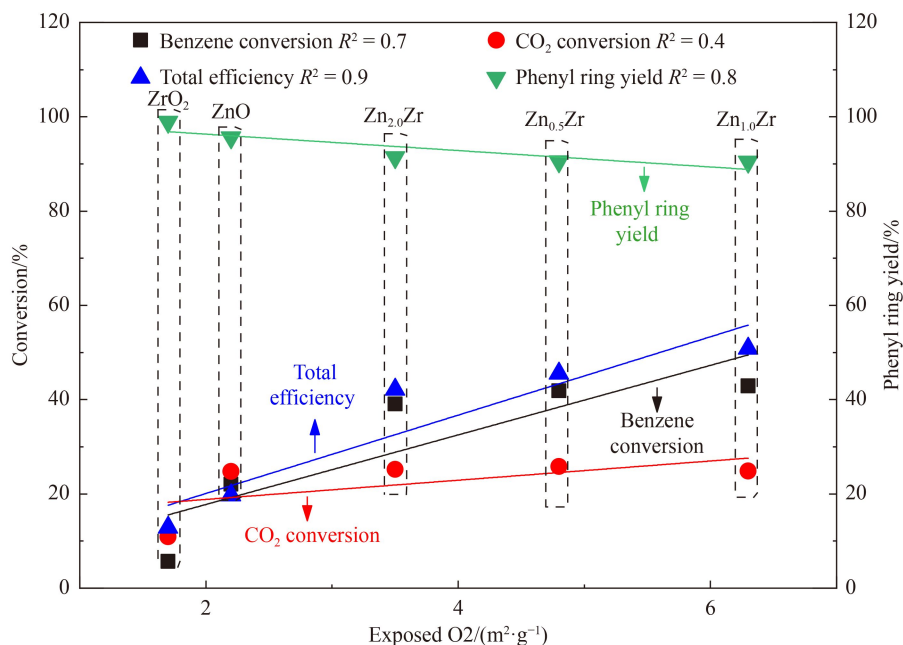
b) Phenyl ring yield = $\frac{\text{Phenyl ring in the product}}{\text{Phenyl ring in the reactant}} = \left[\frac{m_{\text{effluent}}}{(1 - \text{Conv}_{\text{benz}}) M_{\text{benz}} + \sum \text{Conv}_{\text{benz}} \times \text{Select}_i \times M_i} \right] \left(\frac{m_{\text{Feed}}}{M_{\text{benz}}} \right)$; c) EBZ means ethylbenzene; d) PX/X means para-xylene/xylene.

Table 3 Conversion of CO₂ and composition of the gaseous phase^{a)}

Catalyst	CO ₂ conversion/%	Selectivity/%						CO ₂ efficiency ^{b)/%}	Carbon balance/%
		CO	CH ₄	C ₂	C ₃	C ₄₊	EBZ+C ₉₊		
ZrO ₂ -ZSM-5	10.9	84.1	1.6	0.1	0.0	0.1	1.2	12.9	99.5
Zn _{0.5} Zr-ZSM-5	25.8	42.8	0.5	0.1	0.5	0.4	11.1	44.7	97.4
Zn _{1.0} Zr-ZSM-5	23.3	35.8	0.4	0.0	0.4	0.2	12.3	50.9	96.9
Zn _{2.0} Zr-ZSM-5	25.2	46.4	0.5	0.2	0.6	0.5	9.8	42.2	97.9
ZnO-ZSM-5	24.7	72.1	0.8	0.1	0.5	0.6	2.6	23.4	98.6

a) Reaction conditions were the same as those in Table 2;

b) CO₂ efficiency = $\frac{\text{CO}_2 \text{ transferred into toluene and xylene}}{\text{converted CO}_2} = \frac{\text{Feed}_{\text{benz}} \text{Conv} (1 \times \text{Select}_{\text{tol}} + 2 \times \text{Select}_{\text{xy}})}{\text{Feed}_{\text{CO}_2} \times \text{Conv}_{\text{CO}_2}}$.

**Fig. 6** Relationship between exposed O₂ and catalytic activity of Zn_xZr oxides.

3.2.2 Stability tests

The catalytic stability of Zn_{1.0}Zr-ZSM-5 in the alkylation of benzene and CO₂ with H₂ was studied. The reaction conditions are the same as Table 2. It is apparent from Fig. 7 that the conversion and selectivity of the composite catalyst do not change significantly, indicating that the

composite catalyst possesses a good stability in an 80 h test.

3.3 Investigation of reaction mechanism

To further explore the reaction pathways, *in-situ* infrared

spectroscopy was used to monitor the surface species produced in the reaction (Fig. 8). Peak attribution is confirmed in Table S1. The reaction conditions for the experiment (a) were 325 °C, 0.6 MPa, and the reaction gas (H₂:CO₂ = 3:1) was introduced at a rate of 10 mL·min⁻¹ into the *in-situ* cell containing the catalyst. In Fig. 8, the results show the appearance of characteristic peaks for CH₃O* (2826 and 2933 cm⁻¹) as well as for HCOO* (2882, 1382, 1370, and 1585 cm⁻¹) indicating the formation of HCOO* and CH₃O* on the oxide by the mixture of carbon dioxide and hydrogen. The bands at 2882 cm⁻¹ and 2826 cm⁻¹ are chosen to study the dynamics of HCOO* and CH₃O* at 325 °C (Fig. S1). Both intermediates grew rapidly at first and then gradually leveled off.

To further explore the reaction pathway of benzene alkylation with CO₂, the mechanism of the evolution of Zn_{1.0}Zr-ZSM-5 in the reaction at 0.6 MPa and 325 °C

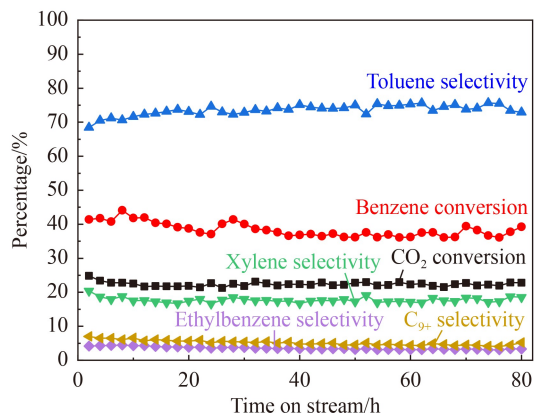


Fig. 7 Stability of Zn_{1.0}Zr-ZSM-5 catalyst in ABCH reaction.

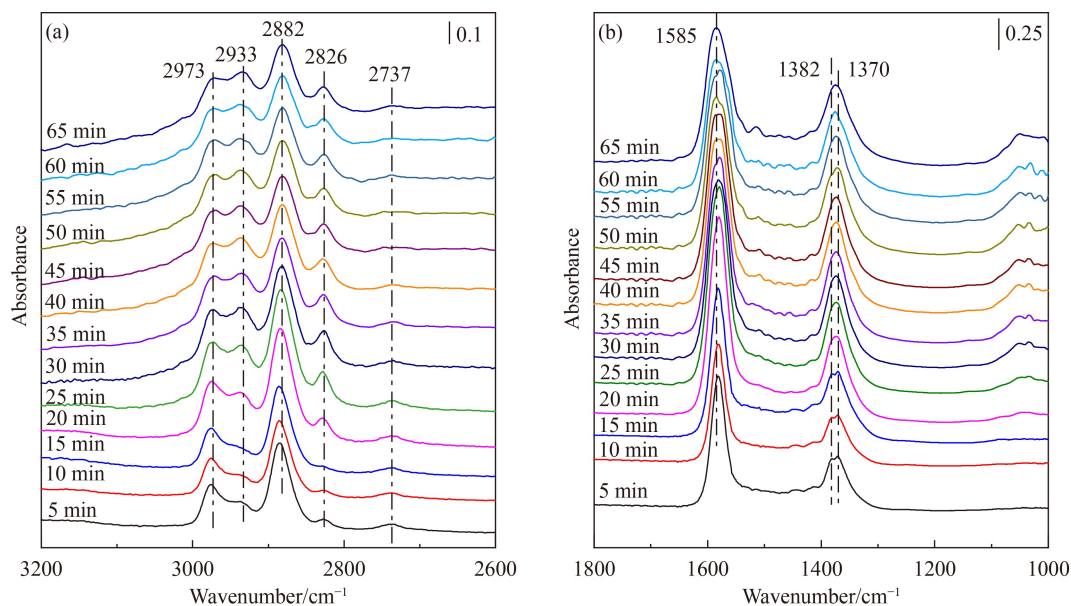


Fig. 8 Time-resolved *in-situ* infrared spectra of Zn_{1.0}Zr under 0.6 MPa CO₂ + H₂ (H₂:CO₂ = 3) atmosphere at 325 °C: (a) wavenumber 3200–2600 cm⁻¹; (b) wavenumber 1800–1000 cm⁻¹.

was investigated by *in-situ* infrared spectroscopy (Fig. 9). A mixture of CO₂ and H₂ gas (10 mL·min⁻¹, H₂:CO₂ = 3:1) was first passed into the reaction cell of unreacted Zn_{1.0}Zr-ZSM-5 catalyst for 30 min, followed by a purge with argon for 10 min (experiments (a1, a2)), where HCOO* and CH₃O* peaks appeared. Subsequently, the gas was switched to benzene saturated argon (10 mL·min⁻¹) into the *in-situ* cell (experiments (b1, b2)) and the characteristic peaks for HCOO* and CH₃O* species faded and disappeared completely, indicating that the HCOO* and CH₃O* had been consumed by benzene. Benzene saturated mixture of CO₂ and H₂ were simultaneously passed into the reaction cell (experiments (c1, c2)), but no production from alkylbenzene was detected during this process, probably due to the low amount of alkylbenzene produced.

Experiments such as the *in-situ* infrared described above demonstrated that the ABCH proceeded in two steps (Fig. 10). Carbon dioxide chemisorbed on oxygen vacancies to produce carbonate/bicarbonate species, which then underwent progressive hydrogenation to give COOH*, CH₃O* and finally methanol, and these intermediate species were rapidly transferred to the acidic site of HZSM-5 to produce target products such as toluene xylene by reaction with benzene.

4 Conclusions

In summary, a bifunctional catalyst composed of Zn_xZr and ZSM-5 was developed for ABCH reaction to toluene and xylene directly through a tandem catalysis process. Zn/Zr solid solution owning a cubic ZrO₂ shell rich in Zn

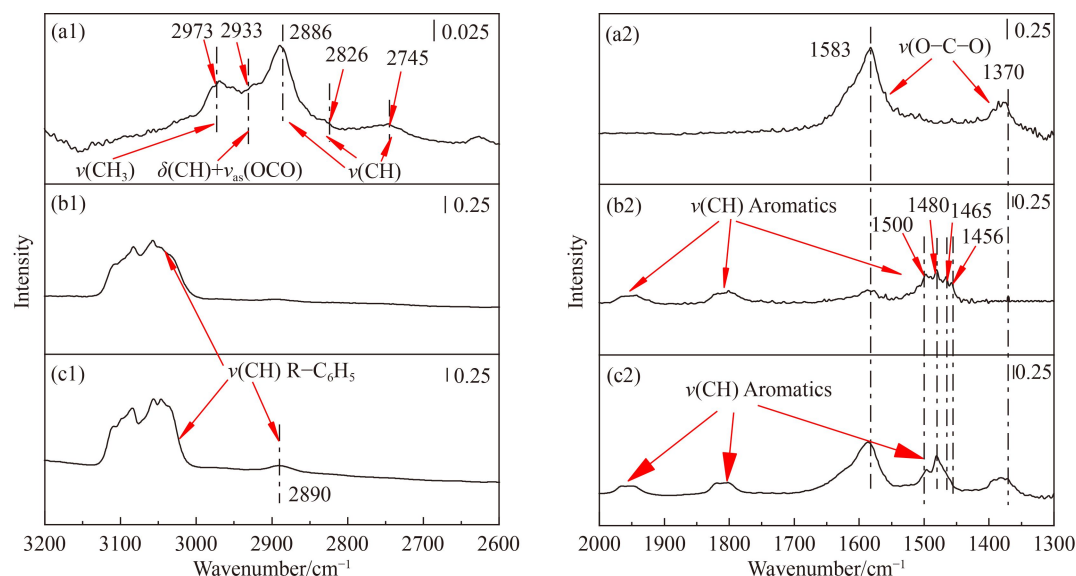


Fig. 9 *In-situ* infrared spectra of $\text{Zn}_{1.0}\text{Zr}$ -ZSM-5 catalyst recorded at 325 °C under 0.6 MPa: (a1, b1, c1) wavenumber 3200–2600 cm^{-1} ; (a2, b2, c2) wavenumber 2000–1300 cm^{-1} .

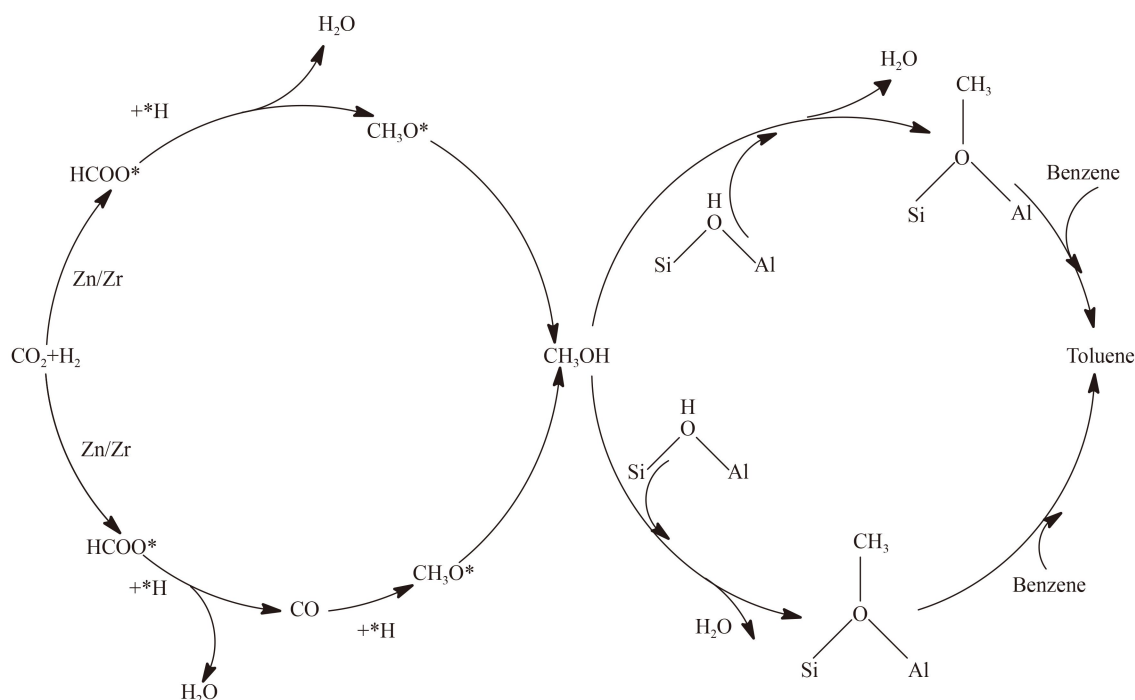


Fig. 10 Reaction mechanism diagram.

and monoclinic ZrO_2 core was formed with a Zn/Zr ratio of 1:1. The unique structure grants it abundant oxygen vacancies which result in fabulous reaction performances, displaying benzene conversion of 42.9% and total toluene/xylene selectivity of 90.0%. In addition, benefiting from the special structure, more than 50% of carbon dioxide was effectively utilized and incorporated into the target product as a consequence of refrained reverse water gas shift reaction. The bifunctional catalyst $\text{Zn}_x\text{Zr}/\text{ZSM-5}$ also exhibited excellent stability, and no catalyst

deactivation was observed in 80 h long-term stability test. More importantly, the mechanism study reveals that carbon dioxide chemisorbs on the oxygen vacancies of Zn_xZr to form carbonate/bicarbonate species, which subsequently undergo stepwise hydrogenation to give HCOO^* and CH_3O^* . These intermediates are rapidly transferred to the acidic site of HZSM-5 to produce target products. This report provides a very promising strategy for the utilization of CO_2 , by which we can realize more conversion of CO_2 to value-added chemical synthesis.

Acknowledgments This project was sponsored financially by the National Natural Science Foundation of China (Grant No. 21776076) and the Fundamental Research Funds for the Central Universities (Grant No. JKA01211710).

Electronic Supplementary Material Supplementary material is available in the online version of this article at <https://dx.doi.org/10.1007/s11705-022-2215-6> and is accessible for authorized users.

References

1. Zhong J, Yang X, Wu Z, Liang B, Huang Y, Zhang T. State of the art and perspectives in heterogeneous catalysis of CO₂ hydrogenation to methanol. *Chemical Society Reviews*, 2020, 49(5): 1385–1413
2. Bushuyev O S, De Luna P, Dinh C T, Tao L, Saur G, Van De Lagemaat J, Kelley S O, Sargent E H. What should we make with CO₂ and how can we make it? *Joule*, 2018, 2(5): 825–832
3. Bonura G, Cordaro M, Cannilla C, Mezzapica A, Spadaro L, Arena F, Frusteri F. Catalytic behaviour of a bifunctional system for the one step synthesis of DME by CO₂ hydrogenation. *Catalysis Today*, 2014, 228: 51–57
4. Kattel S, Liu P, Chen J G. Tuning selectivity of CO₂ hydrogenation reactions at the metal/oxide interface. *Journal of the American Chemical Society*, 2017, 139(29): 9739–9754
5. Liu J, Zhang A, Jiang X, Liu M, Sun Y, Song C, Guo X. Selective CO₂ hydrogenation to hydrocarbons on Cu-promoted Fe-based catalysts: dependence on Cu–Fe interaction. *ACS Sustainable Chemistry & Engineering*, 2018, 6(8): 10182–10190
6. Wang J, You Z, Zhang Q, Deng W, Wang Y. Synthesis of lower olefins by hydrogenation of carbon dioxide over supported iron catalysts. *Catalysis Today*, 2013, 215(41): 186–193
7. Bonura G, Cordaro M, Spadaro L, Cannilla C, Arena F, Frusteri F. Hybrid Cu-ZnO-ZrO₂/H-ZSM5 system for the direct synthesis of DME by CO₂ hydrogenation. *Applied Catalysis B: Environmental*, 2013, 140-141: 16–24
8. Martin O, Martin A J, Mondelli C, Mitchell S, Segawa T F, Hauert R, Drouilly C, Curulla-Ferre D, Perez-Ramirez J. Indium oxide as a superior catalyst for methanol synthesis by CO₂ hydrogenation. *Angewandte Chemie International Edition*, 2016, 55(21): 6261–6265
9. Xu G, Zhang P, Cheng J, Wei T, Zhu X, Yang F. Preparation of a hollow HZSM-5 zeolite supported molybdenum catalyst by desilication-recrystallization for enhanced catalytic properties in propane aromatization. *Journal of Solid State Chemistry*, 2021, 300(6): 122238–122247
10. Odedairo T, Balasamy R J, Al-Khattaf S. Toluene disproportionation and methylation over zeolites TNU-9, SSZ-33, ZSM-5, and mordenite using different reactor systems. *Industrial & Engineering Chemistry Research*, 2011, 50(6): 3169–3183
11. Lyons T W, Guironnet D, Findlater M, Brookhart M. Synthesis of *p*-xylene from ethylene. *Journal of the American Chemical Society*, 2012, 134(38): 15708–15711
12. Chen Z, Ni Y, Zhi Y, Wen F, Zhou Z, Wei Y, Zhu W, Liu Z. Coupling of methanol and carbon monoxide over H-ZSM-5 to form aromatics. *Angewandte Chemie International Edition*, 2018, 57(38): 12549–12553
13. Dong P, Zhang Y, Li Z, Yong H, Li G, Ji D. Enhancement of the utilization of methanol in the alkylation of benzene with methanol over 3-aminopropyltriethoxysilane modified HZSM-5. *Catalysis Communications*, 2019, 123: 6–10
14. Gao K, Li S, Wang L, Wang W. Study of the alkylation of benzene with methanol for the selective formation of toluene and xylene over Co₃O₄-La₂O₃/ZSM-5. *RSC Advances*, 2015, 5(56): 45098–45105
15. Wang Y, He X, Yang F, Su Z, Zhu X. Control of framework aluminum distribution in MFI channels on the catalytic performance in alkylation of benzene with methanol. *Industrial & Engineering Chemistry Research*, 2020, 59(30): 13420–13427
16. Wang Y, Xu S, He X, Yang F, Zhu X. Regulating the acid sites and framework aluminum siting in MCM-22 zeolite to enhance its performance in alkylation of benzene with methanol. *Microporous and Mesoporous Materials*, 2022, 332: 111677–111688
17. Zhu Z, Chen Q, Zhu W, Kong D, Li C. Catalytic performance of MCM-22 zeolite for alkylation of toluene with methanol. *Catalysis Today*, 2004, 93(9): 321–325
18. Li Y, Yan T, Junge K, Beller M. Catalytic methylation of C–H bonds using CO₂ and H₂. *Angewandte Chemie International Edition*, 2014, 53(39): 10476–10480
19. Ting K W, Kamakura H, Poly S S, Toyao T, Hakim Siddiki S M A, Maeno Z, Matsushita K, Shimizu K I. Catalytic methylation of aromatic hydrocarbons using CO₂/H₂ over Re/TiO₂ and H-MOR catalysts. *ChemCatChem*, 2020, 12(8): 2215–2220
20. Ting K W, Kamakura H, Poly S S, Takao M, Siddiki S M A H, Maeno Z, Matsushita K, Shimizu K I, Toyao T. Catalytic methylation of *m*-xylene, toluene, and benzene using CO₂ and H₂ over TiO₂-supported Re and zeolite catalysts: machine-learning-assisted catalyst optimization. *ACS Catalysis*, 2021, 11(9): 5829–5838
21. Ting K W, Imbe T, Kamakura H, Maeno Z, Siddiki S M A H, Matsushita K, Shimizu K I, Toyao T. Catalytic methylation of benzene over Pt/MoO_x/TiO₂ and zeolite catalyst using CO₂ and H₂. *Chemistry Letters*, 2022, 51(2): 149–152
22. Zuo J, Chen W, Liu J, Duan X, Yuan Y. Selective methylation of toluene using CO₂ and H₂ to *para*-xylene. *Science Advances*, 2020, 6(34): eaba5433
23. Miao D, Pan X, Jiao F, Ji Y, Hou G, Xu L, Bao X. Selective synthesis of *para*-xylene and light olefins from CO₂/H₂ in the presence of toluene. *Catalysis Science & Technology*, 2021, 11(13): 4521–4528
24. Liu X, Pan Y, Zhang P, Wang Y, Xu G, Su Z, Zhu X, Yang F. Alkylation of benzene with carbon dioxide to low-carbon aromatic hydrocarbons over bifunctional Zn–Ti/HZSM-5 catalyst. *Frontiers of Chemical Science and Engineering*, 2021, 16(3): 384–396
25. Liu C, Lee S, Su D, Zhang Z, Pfefferle L, Haller G L. Synthesis and characterization of nanocomposites with strong interfacial interaction: sulfated ZrO₂ nanoparticles supported on multiwalled carbon nanotubes. *Journal of Physical Chemistry C*, 2012, 116(41): 21742–21752
26. Shannon R D. Revised effective ionic radii and systematic studies

- of interatomic distances in halides and chalcogenides. *Acta Crystallographica Section A*, 1976, 32(5): 751–767
27. Deng X, Lü M, Meng J. Effect of heavy doping of nickel in compound Mo_3Sb_7 : structure and thermoelectric properties. *Journal of Alloys and Compounds*, 2013, 577(15): 183–188
 28. Kumar N, Kishan H, Rao A, Awana V P S. Fe ion doping effect on electrical and magnetic properties of $\text{La}_{0.7}\text{Ca}_{0.3}\text{Mn}_{1-x}\text{Fe}_x\text{O}_3$ ($0 \leq x \leq 1$). *Journal of Alloys and Compounds*, 2010, 502(2): 283–288
 29. Xie S, Iglesia E, Bell A T. Water-assisted tetragonal-to-monoclinic phase transformation of ZrO_2 at low temperatures. *Chemistry of Materials*, 2000, 12(8): 2442–2447
 30. Li M, Feng Z, Ying P, Xin Q, Li C. Phase transformation in the surface region of zirconia and doped zirconia detected by UV Raman spectroscopy. *Physical Chemistry Chemical Physics*, 2003, 5(23): 5326–5332
 31. Song H, Laudenschleger D, Carey J J, Ruland H, Nolan M, Muhler M. Spinel-structured ZnCr_2O_4 with excess Zn is the active $\text{ZnO}/\text{Cr}_2\text{O}_3$ catalyst for high-temperature methanol synthesis. *ACS Catalysis*, 2017, 7(11): 7610–7622
 32. Dong J J, Zhang X W, You J B, Cai P F, Yin Z G, An Q, Ma X B, Jin P, Wang Z G, Chu P K. Effects of hydrogen plasma treatment on the electrical and optical properties of ZnO films: identification of hydrogen donors in ZnO. *ACS Applied Materials & Interfaces*, 2010, 2(6): 1780–1784
 33. Wang J, Li G, Li Z, Tang C, Feng Z, An H, Liu H, Liu T, Li C. A highly selective and stable $\text{ZnO}-\text{ZrO}_2$ solid solution catalyst for CO_2 hydrogenation to methanol. *Science Advances*, 2017, 3(10): e1701290
 34. Chai Y, Li L, Lu J, Li D, Shen J, Zhang Y, Liang J, Wang X. Germanium-substituted Zn_2TiO_4 solid solution photocatalyst for conversion of CO_2 into fuels. *Journal of Catalysis*, 2019, 371: 144–152
 35. Xiao F X. Construction of highly ordered ZnO– TiO_2 nanotube arrays (ZnO/TNTs) heterostructure for photocatalytic application. *ACS Applied Materials & Interfaces*, 2012, 4(12): 7055–7063
 36. Liu Y, Xia C, Wang Q, Zhang L, Huang A, Ke M, Song Z. Direct dehydrogenation of isobutane to isobutene over Zn-doped ZrO_2 metal oxide heterogeneous catalysts. *Catalysis Science & Technology*, 2018, 8(19): 4916–4924
 37. Wang B, Chen B, Sun Y, Xiao H, Xu X, Fu M, Wu J, Chen L, Ye D. Effects of dielectric barrier discharge plasma on the catalytic activity of Pt/ CeO_2 catalysts. *Applied Catalysis B: Environmental*, 2018, 238: 328–338
 38. Ou G, Xu Y, Wen B, Lin R, Ge B, Tang Y, Liang Y, Yang C, Huang K, Zu D, Yu R, Chen W, Li J, Wu H, Liu L M, Li Y. Tuning defects in oxides at room temperature by lithium reduction. *Nature Communications*, 2018, 9(1): 1302–1311
 39. Wang N, Li S, Zong Y, Yao Q. Sintering inhibition of flame-made Pd/ CeO_2 nanocatalyst for low-temperature methane combustion. *Journal of Aerosol Science*, 2017, 105: 64–72
 40. Liu X, Wang M, Zhou C, Zhou W, Cheng K, Kang J, Zhang Q, Deng W, Wang Y. Selective transformation of carbon dioxide into lower olefins with a bifunctional catalyst composed of ZnGa_2O_4 and SAPO-34. *Chemical Communications (Cambridge)*, 2018, 54(2): 140–143
 41. Cheng K, Zhou W, Kang J, He S, Shi S, Zhang Q, Pan Y, Wen W, Wang Y. Bifunctional catalysts for one-step conversion of syngas into aromatics with excellent selectivity and stability. *Chem*, 2017, 3(2): 334–347